

# On the role of pressure anisotropy for relativistic stars admitting conformal motion

Farook Rahaman<sup>♡\*</sup>, Mubasher Jamil<sup>†</sup>, Mehedi Kalam<sup>‡</sup>, Kaushik Chakraborty<sup>♡</sup> and Ashis Ghosh<sup>♡</sup>

<sup>♡</sup>Dept. of Mathematics, Jadavpur University, Kolkata-700 032, India

<sup>†</sup>Center for Advanced Mathematics and Physics, National University of Sciences and Technology,  
Peshawar Road, Rawalpindi - 46000, Pakistan

and

<sup>‡</sup>Department of Physics, Netaji Nagar College for Women, Regent Estate, Kolkata-700092, India

October 16, 2009

## Abstract

We investigate the spacetime of anisotropic stars admitting conformal motion. The Einstein field equations are solved using different ansatz of the surface tension. In this investigation, we study two cases in details with the anisotropy as: [1]  $p_t = np_r$  [2]  $p_t - p_r = \frac{1}{8\pi}(\frac{c_1}{r^2} + c_2)$  where,  $n$ ,  $c_1$  and  $c_2$  are arbitrary constants. The solutions yield expressions of the physical quantities like pressure gradients and the mass.

*Keywords:* Anisotropies, Conformal symmetries, Einstein field equations, Strange stars

## 1 Introduction

Most of the stars in the galaxies are the main sequence stars which evolve by burning lighter elements into heavier nuclei. Stars massive than  $\sim 10M_\odot$  explode into supernova

---

\*Corresponding author: farook\_rahaman@yahoo.com

<sup>†</sup>mjamil@camp.edu.pk

<sup>‡</sup>mehedikalam@yahoo.co.in

leaving the core behind which then collapses to form a compact object. The cores are supported by the degenerate pressure of its constituent particles and possess the densities of the relativistic scales i.e.  $R_s = 2GM/rc^2 \sim 1$  (which is the Schwarzschild radius of the star) where  $M$  is the mass and  $r$  is radius of the compact object. At these densities, relativistic effects dominate and the physical quantities like gradients of pressure and mass are determined by the Tolman-Oppenheimer-Volkoff (TOV) equations for an isotropic and homogeneous compact star. In these stars, the matter is found in stable ground state where the quarks are confined inside the hadrons. It is suggested that the quarks if de-confined into individual  $u$ ,  $d$  and  $s$  quarks can also yield a stable ground state of matter, which is called ‘strange matter’ [1]. Stars composed of mostly strange matter are therefore termed as ‘strange stars’ [2] (see [3, 4] for review on this topic). Generally, superdense stars with mass to size ratio exceeding 0.3 are expected to be composed of strange matter [5]. The prime motivation for the existence of strange stars was to explain the exotic phenomena of gamma ray bursts and soft gamma ray repeaters [6, 7]. Now with the observations of the Rossi X-ray Timing Explorer, it is convincingly shown that astrophysical source SAX J1808.4-3658 is more likely a strange star [8]. The transition from the normal hadronic to the strange matter occurs at sufficiently high densities or corresponding low temperatures as  $T \propto V \propto \rho^{-1}$ . These conditions can mostly be found inside the cores of fast rotating pulsars, P-stars (composed of  $u$  and  $d$  quarks and are in  $\beta$  equilibrium with electrons) or magnetic field powered magnetars. The density distribution inside these stars need not be isotropic and homogeneous (as proposed in the TOV model) if strange matter truly exists, then stars composed of entirely strange matter can also be found. Recently several authors have studied compact stars with anisotropic matter distribution [9, 10, 11, 12, 13]. We provide star models admitting conformal motion with different anisotropy.

To search the natural relation between geometry and matter through the Einstein’s Equations, it is useful to use inheritance symmetry. The well known inheritance symmetry is the symmetry under conformal killing vectors (CKV) i.e.

$$L_\xi g_{ik} = \psi g_{ik}, \quad (1)$$

where  $L$  is the Lie derivative operator,  $\xi$  is the four vector along which the derivative is taken and  $\psi$  is the conformal killing vector. Note that if  $\psi = 0$  then Eq. (1) gives the Killing vector, if  $\psi = \text{constant}$  it gives homothetic vector and if  $\psi = \psi(\mathbf{x}, t)$  then it yields conformal vectors. Thus CKV provides a deeper insight into the spacetime geometry. Moreover, if the conformal factor  $\psi = 0$ , it implies that the underlying spacetime is conformally flat which further implies that the Weyl tensor also vanishes. These conformally flat spacetimes represent gravitational fields without the source of matter producing these fields.

The plan of the paper is as follows: In the second section, we model our gravitational system and formulate the field equations. Next, we shall solve these field equations using different ansatz of our parameters. Then we present the graphical representation of our results. Finally we conclude with the discussion of our results.

## 2 The model

The static spherically symmetric spacetime (in geometrical units  $G = 1 = c$  here and onwards) is taken as

$$ds^2 = e^{\nu(r)} dt^2 - e^{\lambda(r)} dr^2 - r^2(d\theta^2 + \sin^2 \theta d\phi^2). \quad (2)$$

The Einstein field equations (EFE) for the above metric are

$$e^{-\lambda} \left[ \frac{\lambda'}{r} - \frac{1}{r^2} \right] + \frac{1}{r^2} = 8\pi\rho, \quad (3)$$

$$e^{-\lambda} \left[ \frac{\nu'}{r} + \frac{1}{r^2} \right] - \frac{1}{r^2} = 8\pi p_r, \quad (4)$$

$$\frac{1}{2}e^{-\lambda} \left[ \frac{1}{2}(\nu')^2 + \nu'' - \frac{1}{2}\lambda'\nu' + \frac{1}{r}(\nu' - \lambda') \right] = 8\pi p_t. \quad (5)$$

Here  $\rho$  is the energy density while  $p_r$  and  $p_t$  are the radial and transverse pressure densities of the fluid. The conformal killing equation (1) becomes

$$L_\xi g_{ik} = \xi_{i;k} + \xi_{k;i} = \psi g_{ik}. \quad (6)$$

The above equations give the following equations as

$$\xi^1 \nu' = \psi, \quad (7)$$

$$\xi^4 = C_1, \quad (8)$$

$$\xi^1 = \frac{\psi r}{2}, \quad (9)$$

$$\xi^1 \lambda' + 2\xi_{,1}^1 = \psi. \quad (10)$$

Integration of Eqs. (7-10) yield

$$e^\nu = C_2^2 r^2, \quad (11)$$

$$e^\lambda = \left( \frac{C_3}{\psi} \right)^2, \quad (12)$$

$$\xi^i = C_1 \delta_4^i + \left( \frac{\psi r}{2} \right) \delta_1^i, \quad (13)$$

where  $C_i$ ,  $i = 1, 2, 3$  are constants of integration. Making use of Eqs. (11-13) in (3-5), we can write

$$\frac{1}{r^2} \left[ 1 - \frac{\psi^2}{C_3^2} \right] - \frac{2\psi\psi'}{rC_3^2} = 8\pi\rho, \quad (14)$$

$$\frac{1}{r^2} \left[ 1 - \frac{3\psi^2}{C_3^2} \right] = -8\pi p_r, \quad (15)$$

$$\left[ \frac{\psi^2}{C_3^2 r^2} \right] + \frac{2\psi\psi'}{rC_3^2} = 8\pi p_t. \quad (16)$$

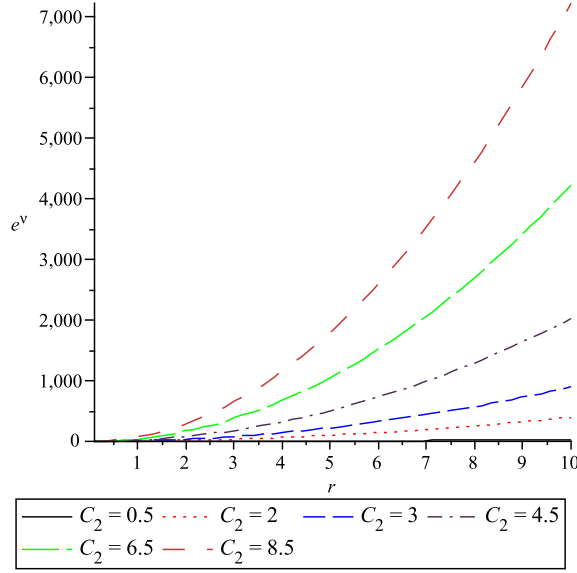


Figure 1: Plot for the variation of  $e^\nu$  vs  $r$ ( km ).

Thus Eqs. (14-16) represent the EFE in terms of the conformal factor  $\psi$  [9, 10, 14]. It is generally assumed that stars are the spherically symmetric anisotropic fluid, so one has to use the equations (2) - (6) for the initial consideration. Since we consider anisotropic star model admitting conformal motion, so all the parameters  $e^\nu$ ,  $e^\lambda$ ,  $\rho$ ,  $p_r$ ,  $p_t$  could be found in terms of conformal factor  $\psi$ . In other words, unless one knows the exact form of  $\psi$ , one could not say anything (i.e. all the physical properties of the anisotropic fluid). Our model is new and interesting in the sense that we are the first authors who consider anisotropic stars with different form of anisotropy admitting conformal motion. The assumption of different anisotropy leads to different differential equations of conformal factor  $\psi$  i.e.  $\psi$  is constrained by the role of anisotropy. Recent observations on highly compact objects like X-ray pulsar Her X-1, etc support the existence of anisotropic stars. But it is still unknown whether stars maintain what type of anisotropy. Since, conformal killing vector provides a deeper insight into the space-time geometry, so we propose anisotropic star models with different anisotropy admitting conformal motion. In the next section, we shall solve these conformal field equations using different ansatz of the surface tension  $p_t - p_r$ . The surface tension actually determines the anisotropy in the stellar model.

### 3 Solution of Conformal EFE

Now we consider three different cases to get exact analytical solutions. Since the metric coefficient  $g_{tt}$  is independent of conformal factor  $\psi$ , so all the cases  $g_{tt}$  assume the same form.

### 3.1 $p_t = np_r$ , $0 < n < 1$ .

The first case deals when  $p_r$  and  $p_t$  are linearly proportional to each other. It is assumed that  $p_t$  is smaller than  $p_r$ . By using above anisotropic relation, Eqs. (15) and (16) together will give a non-homogeneous and non-linear differential equation as

$$\frac{2\psi'r}{\psi} + \frac{nC_3^2}{\psi^2} = (3n - 1). \quad (17)$$

Solving this equation, we get

$$\psi = \sqrt{\left[(rB)^{3n-1} + \frac{nC_3^2}{3n-1}\right]}, \quad (18)$$

where  $B$  is the constant of integration and will be determined later. Hence we get the exact analytical form all the parameters as

$$p_t = \frac{n[C_3^2 + 3(3n-1)(rB)^{(3n-1)}]}{8\pi C_3^2(3n-1)r^2}, \quad (19)$$

$$p_r = \frac{[C_3^2 + 3(3n-1)(rB)^{(3n-1)}]}{8\pi C_3^2(3n-1)r^2}, \quad (20)$$

$$e^\nu = C_2^2 r^2 \quad (21)$$

$$e^\lambda = \frac{C_3^2}{\left[(rB)^{3n-1} + \frac{nC_3^2}{3n-1}\right]}, \quad (22)$$

$$\rho = \frac{1}{8\pi r^2} - \frac{\left[(rB)^{3n-1} + \frac{nC_3^2}{3n-1}\right]}{8\pi C_3^2 r^2} - \frac{[B(3n-1)(rB)^{3n-2}]}{8\pi C_3^2 r}. \quad (23)$$

Differentiation of Eq. (20) with respect to  $r$  yields the pressure gradient

$$8\pi \frac{dp_r}{dr} = \frac{[3B(3n-1)^2(rB)^{(3n-2)}]}{C_3^2(3n-1)r^2} - \frac{2[C_3^2 + 3(3n-1)(rB)^{(3n-1)}]}{C_3^2(3n-1)r^3}. \quad (24)$$

Here, one can note that the pressure gradient is a decreasing function of  $r$  ( see figure 9). In order to get some physically meaningful solution, we need to determine the constant  $B$ . Since vanishing of radial pressure at the boundary is a consequence of the junction condition [15], so one can use

$$p_r(r = R) = 0. \quad (25)$$

to find the constant  $B$ .

Notice that Eq. (25) is motivated due to the fact that pressure gradient is a decreasing function of  $r$ . Thus using Eq. (20) in (25) yields

$$B = \frac{1}{R} \left[ \frac{C_3^2}{3(1-3n)} \right]^{\frac{1}{3n-1}}. \quad (26)$$

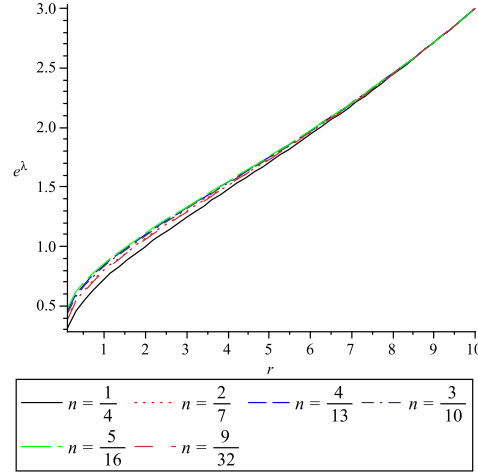


Figure 2: Plot for the variation of  $e^\lambda$  vs  $r$  ( km ). Here we assume the radius of the star  $R = 10$  km and  $C_3 = 1$ .

Using Eq. (26) in (18), we get

$$\psi = \sqrt{\frac{nC_3^2}{1-3n} + \left[ \frac{3^{\frac{1}{1-3n}} \left( \frac{C_3^2}{1-3n} \right)^{\frac{1}{3n-1}} r}{R} \right]^{3n-1}}. \quad (27)$$

The mass function is

$$m(r) = \int_0^r 4\pi\rho r^2 dr = \frac{r(2n-1)}{2(3n-1)} - \frac{(rB)^{3n}}{2BC_3^2}. \quad (28)$$

Thus using Eq. (26) in (28) we obtain

$$m(r) = \frac{r(2n-1)}{2(3n-1)} - \frac{Rr^{3n}}{2C_3^2} \left( \frac{C_3^2}{3-9n} \right)^{\frac{1}{1-3n}} \left[ \frac{\left( \frac{C_3^2}{3-9n} \right)^{\frac{1}{3n-1}} r}{R} \right]^{3n}. \quad (29)$$

Since for  $n \geq \frac{1}{3}$ , the solutions are inconsistent, so we neglect the cases  $n \geq \frac{1}{3}$ . We also observe that  $r = 0$  gives a singularity. However, the solutions are valid for some radius  $r > 0$ . Now, we calculate the subluminal sound speed,  $|v_s^2| = \left| \frac{dp}{d\rho} \right|$  as

$$|v_s^2| = \frac{2[C_3^2 + 3(3n-1)^2(rB)^{3n-1}] - 3(3n-1)^2(rB)^{3n-1}}{3n(3n-1)^2(rB)^{3n-1} + 2(3n-1)C_3^2 - 2(3n-1)(rB)^{3n-1} - 2nC_3^2 - 2(3n-1)^2(rB)^{3n-1}}$$

The above expression should be less than one depending on the parameters. Thus sound speed does not exceed that of light as fulfillment of causality condition.

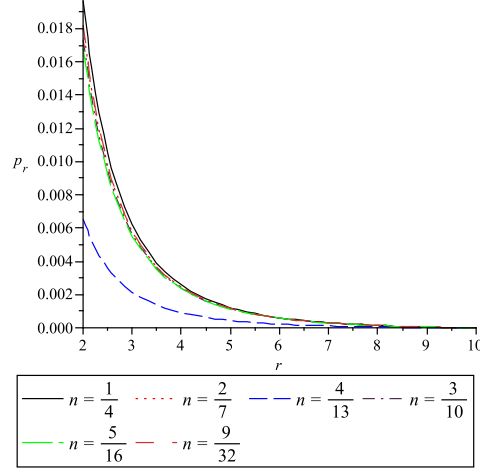


Figure 3: Plot for the variation of radial pressure  $p_r$  vs  $r$ ( km ). Here we assume the radius of the star  $R = 10$  km and  $C_3 = 1$ .

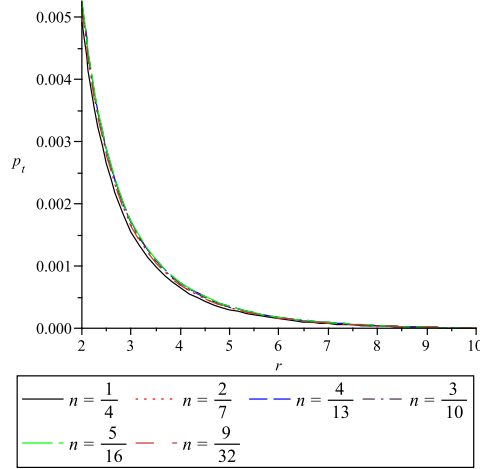


Figure 4: Plot for the variation of transverse pressure  $p_t$  vs  $r$ ( km ). Here we assume the radius of the star  $R = 10$  km and  $C_3 = 1$ .

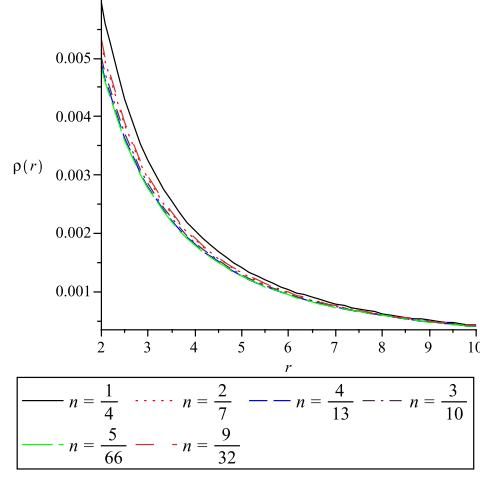


Figure 5: Plot for the variation of energy density  $\rho$  vs  $r$ ( km ). Here we assume the radius of the star  $R = 10$  km and  $C_3 = 1$ .

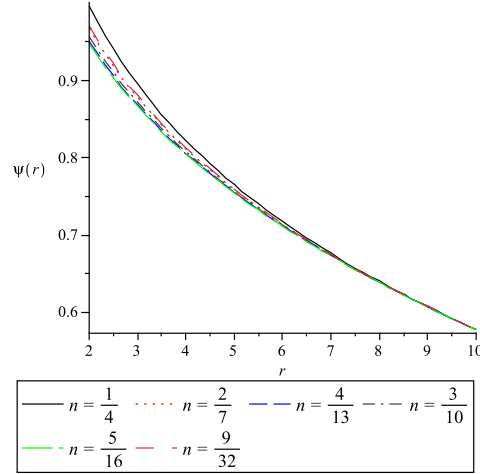


Figure 6: Plot for the variation of the conformal factor  $\psi$  vs  $r$ ( km ). Here we assume the radius of the star  $R = 10$  km and  $C_3 = 1$ .



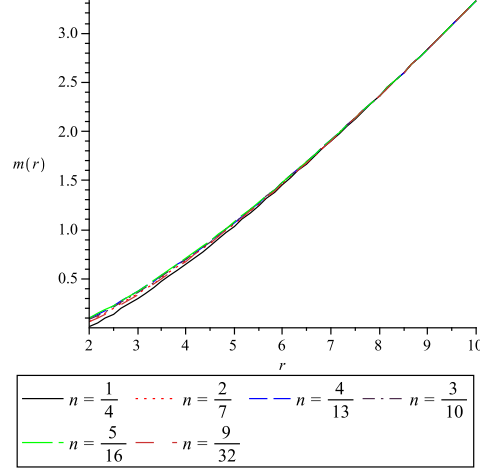


Figure 7: Plot for the variation of mass  $m(r)$  vs  $r$ ( km ). Here we assume the radius of the star  $R = 10$  km and  $C_3 = 1$ .

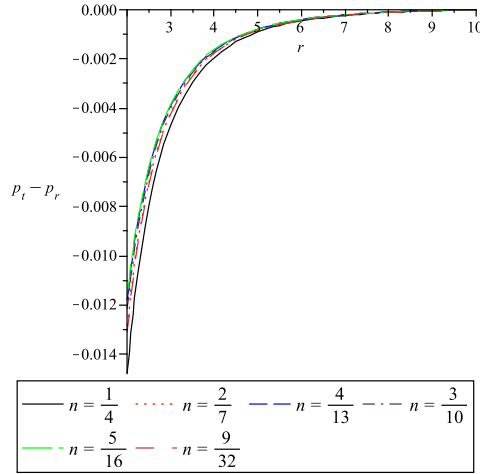


Figure 8: Plot for the variation of the pressure anisotropy  $p_t - p_r$  vs  $r$ ( km ). Here we assume the radius of the star  $R = 10$  km and  $C_3 = 1$ .

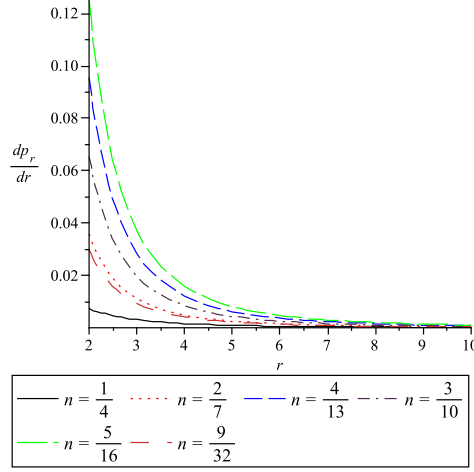


Figure 9: Plot for the variation of the gradient of radial pressure  $\frac{dp_r}{dr}$  vs  $r$  ( km ). Here we assume the radius of the star  $R = 10$  km and  $C_3 = 1$ .

### 3.2 $p_t - p_r = \frac{1}{8\pi}(\frac{c_1}{r^2} + c_2)$ , where $c_1$ and $c_2$ are arbitrary constants.

By using above anisotropic relation [7], we get from Eqs. (15) and (16)

$$\frac{2\psi\psi'}{C_3^2 r} - \frac{2\psi^2}{C_3^2 r^2} = \frac{(c_1 - 1)}{r^2} + c_2. \quad (30)$$

Solving this equation, we get

$$\psi = \sqrt{-\frac{A}{2} + Br^2 \ln r + K_1 r^2}, \quad (31)$$

where  $A = C_3^2(c_1 - 1)$ ,  $B = C_3^2 c_2$  and  $K_1$  is an integration constant. Thus we get the exact analytical form of all the parameters as

$$p_t = \frac{[-A + 4Br^2 \ln r + 2B + 4K_1 r^2]}{16\pi C_3^2 r^2}, \quad (32)$$

$$p_r = \frac{3(-\frac{A}{2} + Br^2 \ln r + K_1 r^2)}{8\pi C_3^2 r^2} - \frac{1}{8\pi r^2}, \quad (33)$$

$$e^\nu = C_2^2 r^2, \quad (34)$$

$$e^\lambda = \frac{C_3^2}{[-\frac{A}{2} + Br^2 \ln r + K_1 r^2]}, \quad (35)$$

$$\rho = \frac{[A - 6Br^2 \ln r - 2Br^2 - 6K_1 r^2 + 2C_3^2]}{16\pi C_3^2 r^2}. \quad (36)$$

$$(37)$$

The mass function is

$$m(r) = \frac{\left[Ar - \frac{2Br^3}{3} - 2K_1 r^3 + 2C_3^2 r - 3Br^3(\ln r - \frac{1}{3})\right]}{4C_3^2}. \quad (38)$$

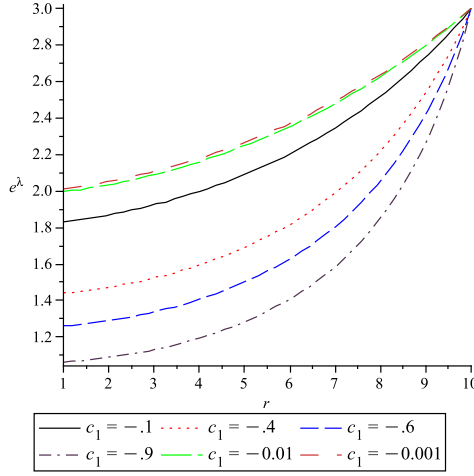


Figure 10: Plot for the variation of  $e^\lambda$  vs  $r$  ( km ). Here we assume the radius of the star  $R = 10$  km with  $c_2 = .001$  and  $C_3 = 1$ .

The pressure gradient is given by

$$\frac{dp_r}{dr} = -\frac{3(-\frac{A}{2} + Br^2 \ln r + K_1 r^2)}{4\pi C_3^2 r^3} + \frac{3(2Br \ln r + Br + 2K_1 r)}{8\pi C_3^2 r^2} + \frac{1}{4\pi r^3}. \quad (39)$$

Applying the similar procedure as done in the previous section,  $p_r(r = R) = 0$  gives

$$K_1 = \frac{1}{R^2} \left[ \frac{C_3^2}{3} + \frac{A}{2} - BR^2 \ln R \right] = \frac{C_3^2}{R^2} \left[ \frac{c_1}{2} - \frac{1}{6} - c_2 R^2 \ln R \right]. \quad (40)$$

As before, we calculate the subluminal sound speed ,  $|v_s^2| = \left| \frac{dp}{d\rho} \right|$  as

$$|v_s^2| = \frac{6(Br^2 \ln r + K_1 r^2 - \frac{A}{2}) - 2C_3^2 - 3r^2(2B \ln r + B + 2K_1)}{r^2(6B \ln r + 5B + 6K_1) + (A - 6Br^2 \ln r - 2Br^2 - 6K_1 r^2 + 2C_3^2)}$$

The above expression should be less than one depending on the parameters. Thus sound speed does not exceed that of light as fulfillment of causality condition.

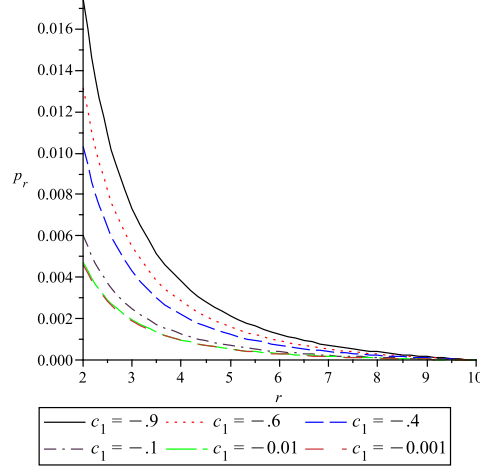


Figure 11: Plot for the variation of radial pressure  $p_r$  vs  $r$ ( km ). Here we assume the radius of the star  $R = 10$  km with  $c_2 = .001$  and  $C_3 = 1$ .

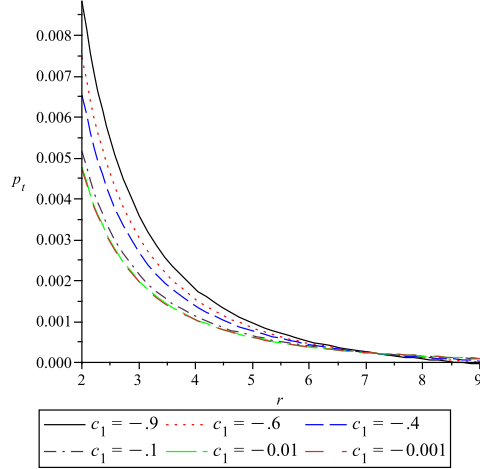


Figure 12: Plot for the variation of transverse pressure  $p_t$  vs  $r$ ( km ). Here we assume the radius of the star  $R = 10$  km with  $c_2 = .001$  and  $C_3 = 1$ .

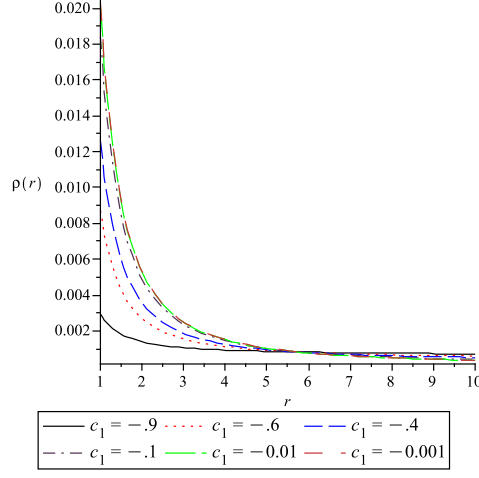


Figure 13: Plot for the variation of energy density  $\rho$  vs  $r$ ( km ). Here we assume the radius of the star  $R = 10$  km with  $c_2 = .001$  and  $C_3 = 1$ .

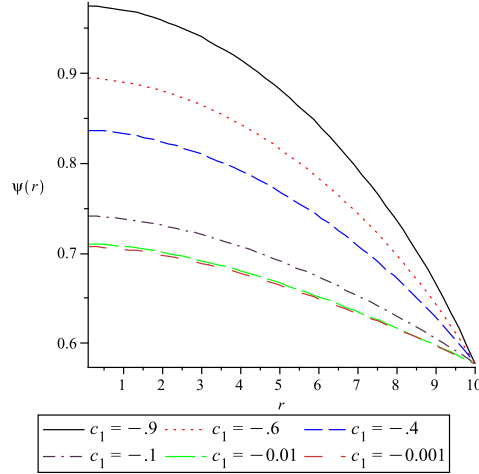


Figure 14: Plot for the variation of the conformal factor  $\psi$  vs  $r$ ( km ). Here we assume the radius of the star  $R = 10$  km with  $c_2 = .001$  and  $C_3 = 1$ .

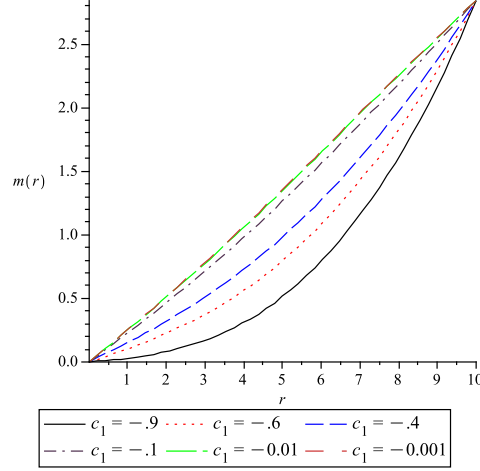


Figure 15: Plot for the variation of mass  $m(r)$  vs  $r$  ( km ). Here we assume the radius of the star  $R = 10$  km with  $c_2 = .001$  and  $C_3 = 1$ .

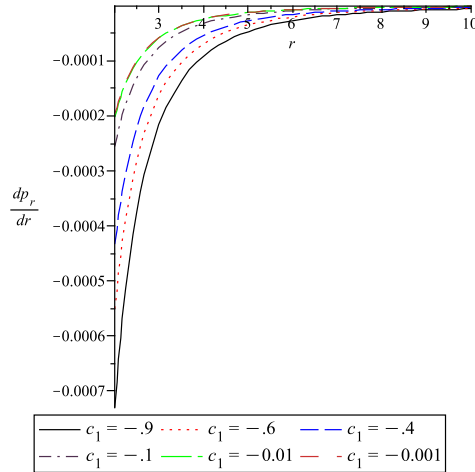


Figure 16: Plot for the variation of the gradient of radial pressure  $\frac{dp_r}{dr}$  vs  $r$  ( km ). Here we assume the radius of the star  $R = 10$  km with  $c_2 = .001$  and  $C_3 = 1$ .

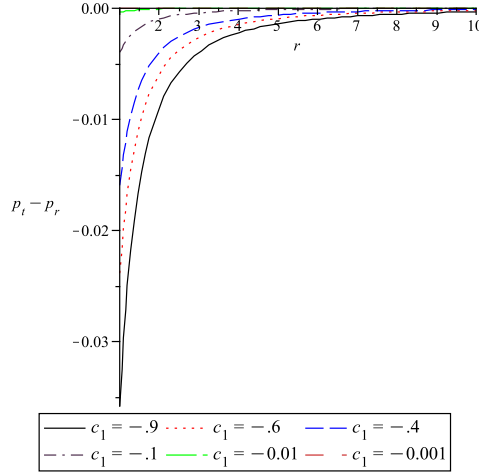


Figure 17: Plot for the variation of the pressure anisotropy  $p_t - p_r$  vs  $r$  ( km ). Here we assume the radius of the star  $R = 10$  km with  $c_2 = .001$  and  $C_3 = 1$ .

## 4 Conclusion and Discussion

In the previous section, we have given the pictorial representation of the parameters involved in the three cases. The constant of integration is fixed at  $C_3 = 1$  while the radius of the compact star is chosen to be  $R = 10$  km. All the other physical parameters like the metric functions  $e^\lambda$  and  $e^\nu$ , radial pressure  $p_r$ , transverse pressure  $p_t$ , surface tension  $p_r - p_t$ , mass function  $m(r)$ , density  $\rho(r)$  and the radial pressure gradient  $dp_r/dr$  are plotted against the radial parameter  $r$  in all the cases.

In figures 1-9, we have taken different values of  $n$  in the range  $(0,1)$  to determine parameters from case-1. We observe that the radial and transverse pressures gradually decrease as  $r$  approaches to the surface  $R$ . This result is consistent with our boundary condition of vanishing pressures all at the stellar surface. It comes as no surprise that the pressure and the mass profile of the compact stars is all along similar to the normal hydrogen burning stars. More specifically, the mass profile of the star shows sharp increase for  $n = \frac{5}{16}$  while it is small for values  $n < \frac{5}{16}$ . The surface tension  $p_t - p_r$  of the star also decreases along with increasing  $r$ . Note that the surface tension varies along negative range due to higher radial pressure. Thus transverse pressure although exists but is smaller than the radial pressure along the allowed range of parameter  $r$ . The pressure gradient  $\nabla_r p_r$  or  $dp_r/dr$  also decreases outward along  $r$ . For small values of parameter  $n$ , the gradient is steeper than for large values. The density profile of the compact star falls for increasing  $r$ . The conformal factor  $\psi(r)$  assumes maximum value at the star's center while it approaches zero near the stellar surface. Therefore, the vanishing conformal factor at the star's surface could be used as an alternative boundary condition for solving conformal field equations.

Similarly, the parameters obtained in case-2 are plotted in figures 10-17 using different values of parameter  $c_1$ . The constant parameter is fixed at  $c_2 = 0.001$ . The pressure profile of the star in this case is similar to the earlier in case-1 having steep slopes with

increasing  $r$ . Also, the density profile and the conformal factor show convergence for large values of  $r$ . The mass profile is steady for  $c_1 = -0.001$  while it is steepest for  $c_1 = -0.9$ . Similarly the declining pressure gradient profile is observed for large  $r$  which is consistent with our boundary condition Eq.(25).

In figures 18-25, we have made a comparison of various stellar parameters obtained in cases 1 and 2. It is observed that the metric function  $e^\lambda$ , conformal factor  $\psi$ , radial pressure  $p_r$  and the transverse pressure  $p_t$  of both cases converge as  $r$  tends to  $R$ . The mass parameter  $m(r)$  is steeper in the second case than the first one. Therefore the mass will increase fast radially in the linear model of the surface tension. Moreover, the surface tension profile of both models goes asymptotically parallel to each other. The density profile in the first case goes to zero while it remains constant in the second case in the asymptotic limit of large  $r$ .

One can note that any static spherically symmetric space time admitting conformal motion suffers  $r = 0$  singularity. In our model also, we had to tolerate  $r = 0$  singularity. Therefore the model does not exist at  $r = 0$ . However, our solutions are valid for some radius  $r > 0$ . We also note that there is a singularity in the mass density, in spite of, the total mass is finite. So, the models ( case - I and case - II ) are physically acceptable. In addition to this, one can find that the matter density and fluid pressure are non negative and gradient  $\frac{dp_r}{dr}$  is decreasing with  $r$ . Thus our models ( i.e. interior solutions of the gravitational field equations ) are fully physically meaningful. As our models suffer  $r = 0$  singularity, the minimum value of  $r$  is taken to be a positive quantity ( km ). Since radius of the star is taken to 10 km ( this is justified as the radius of some of the observed strange stars are nearly equal to 10 km ), so one can note that the total mass of the star is  $m(r=10)$ . Our results have been shown in fig. 7 and fig.15.

In our current analysis, we have used an idealization of spherical symmetry, stationary and static compact star. In general, from the astrophysical point of view, most of the observed or predicted compact star candidates are no longer static but rotating about a unique axis that may be oblique from the magnetic axis of the star. More exotic stars including magnetars (driven by mostly magnetic fields) and pulsars (mostly driven by higher angular momentum) are well known examples of rotating compact stars. In our forth coming work, we plan to work out a similar analysis presented here for the fast rotating or ultra-fast rotating compact stars. We also plan to work on the rotating stars with the slow rotation approximation as well.

## References

- [1] E. Witten, Phys. Rev. D 30 (1984) 272.
- [2] F. DePaolis et al, Int. J. Mod. Phys. D 16 (2007) 827
- [3] R.X. Xu, Acta Astron. Sinica 44 (2003) 245
- [4] N.K. Glendenning, "Compact Stars: Nuclear physics, particle physics and general relativity", (Springer 1997)



- [5] R. Tikekar and K. Jotania, *Pramana J. Phys.* 68 (2007) 397
- [6] K.S. Cheng and Z.G. Dai, *Phys. Rev. Lett.* 80 (1998) 18
- [7] K.S. Cheng and Z.G. Dai, *Phys. Rev. Lett.* 77 (1996) 1210
- [8] X.D. Li et al, *Phys. Rev. Lett.* 83 (1999) 3776.
- [9] A Pradhan et al, gr-qc/0705.4202
- [10] Boehmer C et al, gr-qc/0711.2424
- [11] K. Dev and M. Gleiser, astro-ph/0401546
- [12] R. Sharma and S. D. Maharaj, gr-qc/0708.3317
- [13] I. Yavuz et al, hep-th/0505013
- [14] M. Mak and T. Harko, gr-qc/0309069
- [15] S Chatterjee et al, *Int.J.Theor.Phys.* 32 (1993) 671

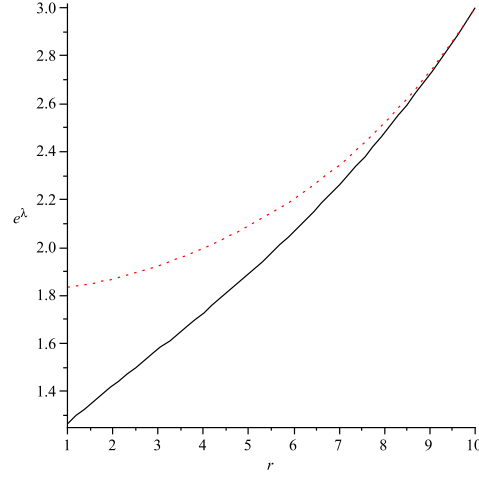


Figure 18: Plot for the variation of  $e^\lambda$  vs  $r$ ( km ). Solid line and dotted line represent the case 1 and case 2 respectively for suitable choices of the parameters.

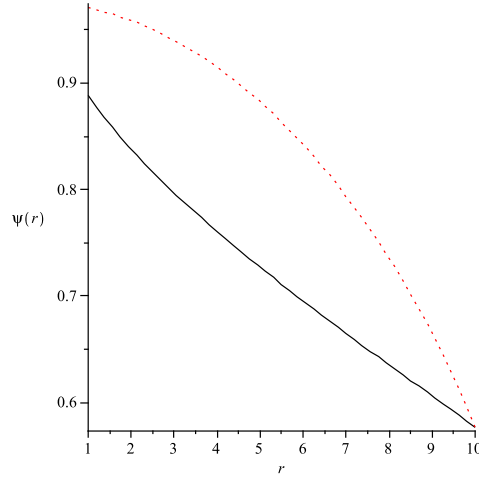


Figure 19: Plot for the variation of conformal factor  $\psi$  vs  $r$ ( km ). Solid line and dotted line represent the case 1 and case 2 respectively for suitable choices of the parameters.

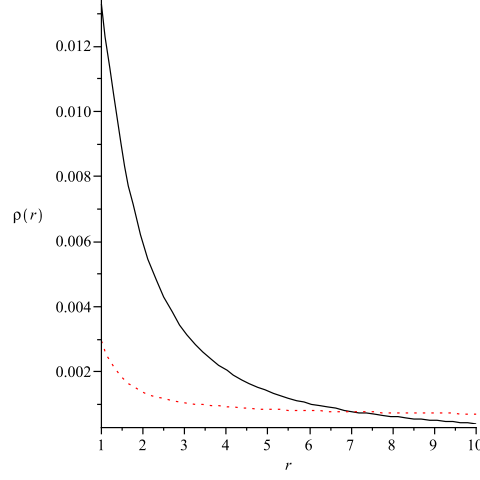


Figure 20: Plot for the variation of energy density  $\rho$  vs  $r$ ( km ). Solid line and dotted line represent the case 1 and case 2 respectively for suitable choices of the parameters.

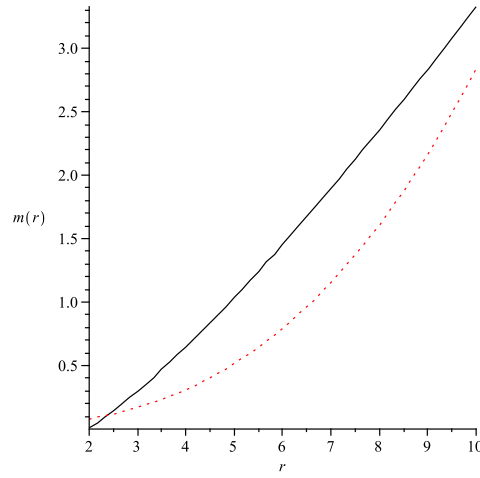


Figure 21: Plot for the variation of mass  $m(r)$  vs  $r$ ( km ). Solid line and dotted line represent the case 1 and case 2 respectively for suitable choices of the parameters.

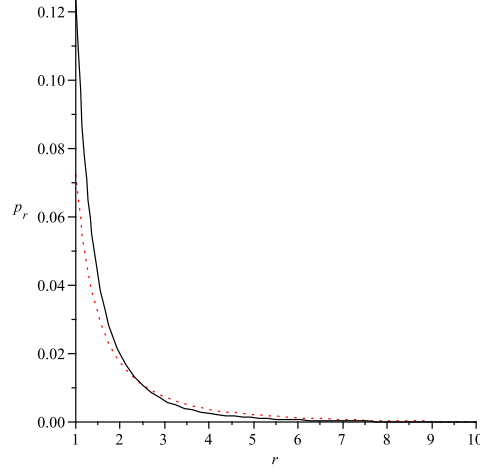


Figure 22: Plot for the variation of the radial pressure  $p_r$  vs  $r$ ( km ). Solid line and dotted line represent the case 1 and case 2 respectively for suitable choices of the parameters.

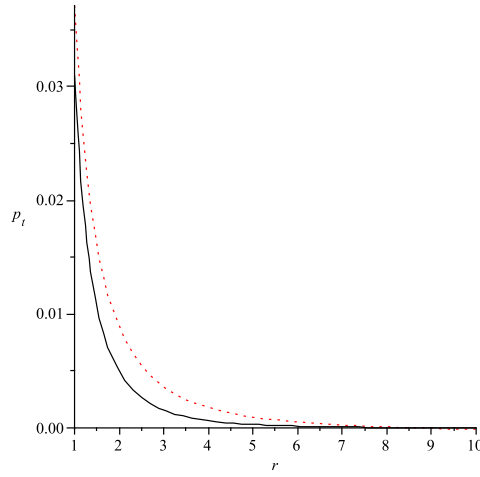


Figure 23: Plot for the variation of the transverse pressure  $p_t$  vs  $r$ (km). Solid line and dotted line represent the case 1 and case 2 respectively for suitable choices of the parameters.

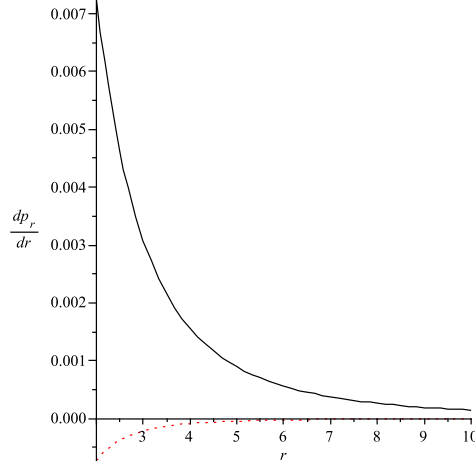


Figure 24: Plot for the variation of the gradient of radial pressure  $\frac{dp_r}{dr}$  vs  $r(\text{km})$ . Solid line and dotted line represent the case 1 and case 2 respectively for suitable choices of the parameters.

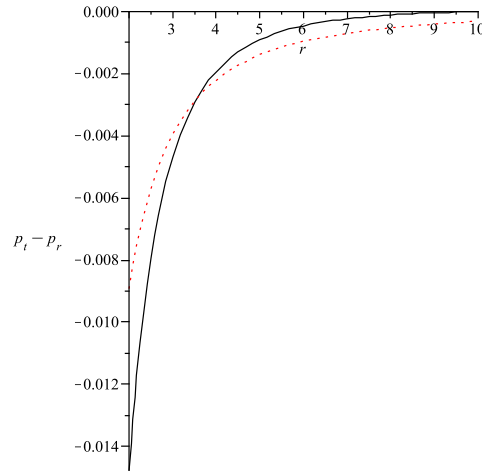


Figure 25: Plot for the variation of the pressure anisotropy  $p_t - p_r$  vs  $r(\text{ km })$ . Solid line and dotted line represent the case 1 and case 2 respectively for suitable choices of the parameters.